Matter

Article

Evolution from topological Dirac metal to flat-band-induced antiferromagnet in layered $K_xNi_4S_2$ ($0 \leq x \leq 1$)

Graphical abstract

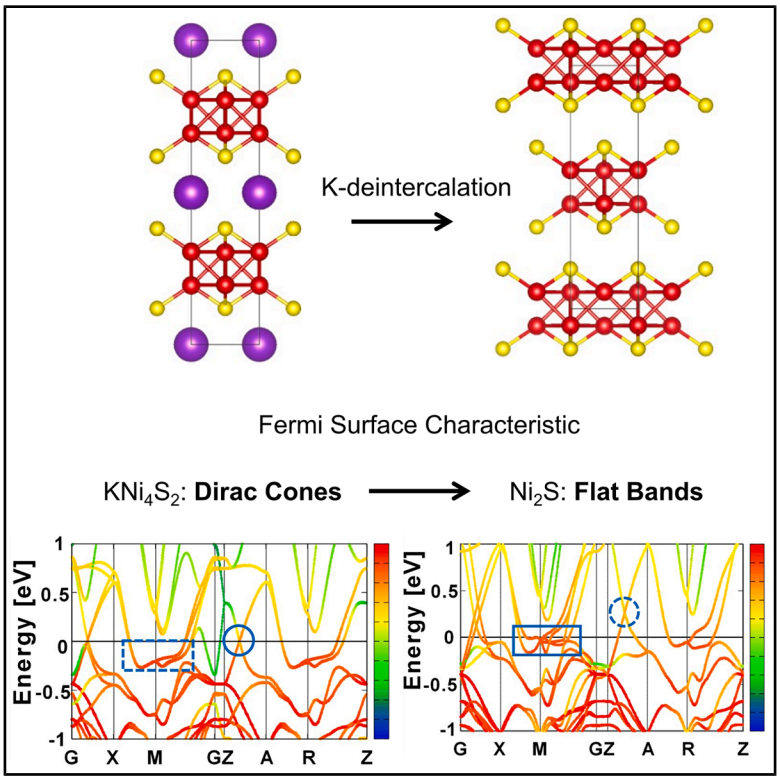

Highlights

- Coexistence of flat bands and Dirac cones without Kagome/honeycomb lattices
- Continuously tunable Fermi surface through topochemical K-deintercalation
- Switchable ground state between Dirac-cone- and flat-band-dominated regimes
- Establishment of a new material design paradigm for correlated topological systems

Authors

Hengdi Zhao, Xiuquan Zhou, Hyowon Park, ..., Duck-Young Chung, Stephan Rosenkranz, Mercouri G. Kanatzidis

Correspondence

m-kanatzidis@northwestern.edu

In brief

Dirac cones with massless fermions and flat bands featuring massive electrons coincide in $K_xNi_4S_2$ ($0 \leq x \leq 1$) and can be accessed selectively by continuous tuning of the Fermi level via topochemical potassium deintercalation. The ability to traverse between a topological Dirac metal and a flat-band-induced antiferromagnet within a single crystalline system, without relying on artificial lattice engineering or exotic structures like Kagome or honeycomb lattices, represents an experimentally validated platform for exploring emergent correlated phenomena.

Zhao et al., 2026, Matter 9, 102418
January 7, 2026
https://doi.org/10.1016/j.matt.2025.102418

1 Discovery
A new material or phenomena

CellPress

Please cite this article in press as: Zhao et al., Evolution from topological Dirac metal to flat-band-induced antiferromagnet in layered $K_xNi_4S_2$ ($0 \leq x \leq 1$), Matter (2025), https://doi.org/10.1016/j.matt.2025.102418

Matter

CellPress

Article

Evolution from topological Dirac metal to flat-band-induced antiferromagnet in layered $K_xNi_4S_2$ ($0 \leq x \leq 1$)

Hengdi Zhao,[1,14] Xiuquan Zhou,[1,2,14] Hyowon Park,[1,3] Tianqi Deng,[4,5] Brandon Wilfong,[6,7] Alann P. Au II,[8] Samuel E. Pate,[1,9] Craig M. Brown,[10] Hui Wu,[10] Tushar Bhowmick,[11] Tessa McNamee,[11] Ravhi Kumar,[3] Yu-Sheng Chen,[12] Zhi-Li Xiao,[1,9] Russell Hemley,[13] Weizhao Cai,[11] Shanti Deemyad,[11] Duck-Young Chung,[1] Stephan Rosenkranz,[1] and Mercouri G. Kanatzidis[1,8,15,*]

[1]Materials Science Division, Argonne National Laboratory, Lemont, IL 60439, USA
[2]Department of Chemistry, Georgetown University, Washington, DC 20057, USA
[3]Department of Physics, University of Illinois at Chicago, Chicago, IL 60607, USA
[4]State Key Laboratory of Silicon and Advanced Semiconductor Materials, School of Materials Science and Engineering, Zhejiang University, Hangzhou, China
[5]Institute of Advanced Semiconductors and Zhejiang Provincial Key Laboratory of Power Semiconductor Materials and Devices, ZJU-Hangzhou Global Scientific and Technological Innovation Center, Zhejiang University, Hangzhou, China
[6]Department of Chemistry, Johns Hopkins University, 3400 N. Charles Street, Baltimore, MD 21218, USA
[7]Institute for Quantum Matter, William H. Miller III Department of Physics and Astronomy, Johns Hopkins University, 3400 N. Charles Street, Baltimore, MD 21218, USA
[8]Department of Chemistry, Northwestern University, Evanston, IL 60208, USA
[9]Department of Physics, Northern Illinois University, DeKalb, IL 60115, USA
[10]NIST Center for Neutron Research, National Institute of Standards and Technology, Gaithersburg, MD 20899, USA
[11]Department of Physics and Astronomy, University of Utah, Salt Lake City, UT 84112, USA
[12]NSF's ChemMatCARS, the University of Chicago, Lemont, IL 60439, USA
[13]Departments of Physics, Chemistry, and Earth and Environmental Sciences, University of Illinois at Chicago, Chicago, IL 60607, USA
[14]These authors contributed equally
[15]Lead contact
*Correspondence: m-kanatzidis@northwestern.edu
https://doi.org/10.1016/j.matt.2025.102418

PROGRESS AND POTENTIAL Dirac materials and flat-band systems, each possessing distinct electronic structures, have captivated a wide range of scientific communities for their potential to host diverse emerging phenomena. In particular, a tunable ground state featuring a Fermi surface dominated by massive fermions from the flat band and massless fermions from the Dirac cone offers an ideal platform to study the interplay between these emerging phenomena. Despite great interest in such systems, materials with coexisting Dirac cones and flat bands are rare, relying on artificial lattice engineering, such as twisted bilayer graphene, or exotic structures, like Kagome or honeycomb lattices. In addition, the lack of an effective method for tuning the Fermi level poses another challenge. Here, we report a layered quantum material, $K_xNi_4S_2$ ($0 \leq x \leq 1$), that simultaneously hosts both flat bands and Dirac cones at distinct energies without involving the typical Kagome or honeycomb lattice. Our molecular orbital bonding analysis suggests that the Ni–Ni bonding exclusively hosted by $K_xNi_4S_2$ plays a vital role in the formation of Dirac cones. Notably, the K-content can be controlled through the K-deintercalation process, enabling the long-sought effective method of wide-range tuning of the Fermi level. With first-principles calculations and experimental confirmation, we demonstrate the versatile ground state that can be fine-tuned through the K-deintercalation process, from a non-magnetic topological Dirac metal (KNi_4S_2, $x = 1$) to a flat-band-induced antiferromagnet (Ni_2S, $x = 0$). The $K_xNi_4S_2$ ($0 \leq x \leq 1$) system offers an experimentally validated, versatile platform for exploring emerging phenomena from massless Dirac fermions, flat-band heavy electrons, and the interplay between them. This *ex situ* topochemical K-deintercalation study also establishes a highly tunable ground state, demonstrating a viable pathway for *in situ* control of quantum materials that can switch between Dirac-cone- and flat-band-dominated states via electrochemical intercalation and deintercalation.

Please cite this article in press as: Zhao et al., Evolution from topological Dirac metal to flat-band-induced antiferromagnet in layered $K_xNi_4S_2$ ($0 \leq x \leq 1$), Matter (2025), https://doi.org/10.1016/j.matt.2025.102418

SUMMARY

Condensed matter systems with coexisting Dirac cones and flat bands and a switchable control between them within a single system are desirable but remarkably uncommon. Here, we report a layered quantum material system, $K_xNi_4S_2$ ($0 \leq x \leq 1$), that simultaneously hosts both characteristics without involving typical Kagome/honeycomb lattices. Enabled by a topochemical K-deintercalation process, the Fermi surface can be fine-tuned continuously over a wide range of energies. Consequently, a non-magnetic Dirac-metal state with a topological nontrivial Z_2 index of 1;(000), supported by first-principles calculations and high mobility up to 1,471 $cm^2V^{-1}s^{-1}$, is observed on the K-rich x = 1 side, whereas a flat-band-induced antiferromagnetic state with T_N up to 10.1 K emerges as the K-content approaches 0. The $K_xNi_4S_2$ system offers a versatile platform for exploring emerging phenomena and underscores a viable pathway for *in situ* control of quantum materials dominated by Dirac cones, flat bands, and their interplay.

INTRODUCTION

Flat bands give rise to massive electrons with a large density of states (DOS), fostering a range of strongly correlated phenomena, including superconductivity,[1–4] magnetism,[5–10] heavy fermion behavior,[11–14] charge density waves,[15] fractional quantum anomalous Hall effects,[16] exceptionally large Seebeck coefficients,[17–19] etc. In contrast, Dirac cones feature linear band dispersions, leading to high carrier mobilities and fractional quantum Hall effects[20,21] due to the vanishing effective mass and contributing minimal DOS to the Fermi surface when the Dirac cone is right at the Fermi level. Dirac cones are typically observed in graphene[22–24] and analogous materials featuring the honeycomb lattice, such as silicene,[25] germanene,[26] and stanene,[27] and topological materials.[28–32]

Materials that exhibit a trivial progression of ground states through systematic doping, where each state is only marginally different from the next, are relatively common. In contrast, materials that can be tuned to access two or more fundamentally distinct electronic ground states, such as switching between a flat-band system with massive carriers and one hosting massless Dirac fermions, are rare and scientifically far more valuable. These systems, where external perturbations can induce qualitative, not merely incremental, transformations in the Fermi surface, present exceptional opportunities for discovering and controlling emergent quantum phenomena. Such coexisting and switchable states have been predicted for cold atoms in optical lattices[33,34] and experimentally realized for polaritons in a photonic lattice in the semiconductor microcavity.[35] However, the experimental realization in a condensed matter system is rare, chiefly because of limited understanding of how to design a system hosting both characteristics simultaneously and, subsequently, how to switch the ground state between them by manipulating the Fermi level. The artificial structure of twisted bilayer graphene offers an experimental demonstration in the condensed matter system, showing the Fermi surface dominated by flat bands near the magic-angle twisting angle, leading to multiple superconducting domes separated by Mott insulating states,[1–4] and by Dirac cones at different twisting angles.[36] As for bulk material systems, the Kagome architecture naturally hosts both flat bands and Dirac cones, as depicted in the nearest-neighbor tight-binding model.[37,38] Despite the rich phenomenology predicted in the Kagome materials, the experimental realization of highly tunable electronic states between Dirac cones and flat bands in bulk Kagome materials remains a challenge.[39,40] Consequently, most experimental and theoretical efforts focus on only one of such characteristics, for example, flat-band-induced correlated phenomena such as magnetism,[41–44] nontrivial band topology from Dirac cones,[42,45] or Van Hove singularity (VHS)-driven electronic instabilities,[46–51] depending on the specific electronic band fillings. Recently, a tunable Fermi level was demonstrated between Ni_3In and Ni_3Sn. However, the replacement of In with Sn shifts the Fermi level further away from all the interesting characteristics.[52] Nevertheless, the ability to finely tune the electronic structure from a Dirac-cone-dominated state to one governed by flat bands within a single system, to our knowledge, has yet to be demonstrated in bulk quantum materials.

Here, we show that the system $K_xNi_4S_2$ ($0 \leq x \leq 1$)[53] simultaneously hosts flat bands and Dirac cones at distinct energies without involving the Kagome or honeycomb lattices. Our molecular orbital (MO) bonding analysis suggests that the Ni–Ni bonding exclusively hosted by $K_xNi_4S_2$ plays a vital role in the formation of Dirac cones. This finding aligns with a symmetry-based analysis demonstrating that the square lattice involving direct Ni–Ni bonding with dominating $d_{x^2-y^2}$ orbitals has the potential to host Dirac cones.[54] On the other hand, the flat band and its associated magnetism originate from the dominant Ni–Ni–$d_{x^2-y^2}$ orbital bonding[53] and Ni–S bonding[55] close to the Fermi level.

Moreover, the potassium content can be controlled through a topotactic K-deintercalation process, providing an effective method to adjust the Fermi level from the higher-lying Dirac state to the lower-lying flat-band state. Both first-principles calculations and experimental evidence validate that the Fermi level and the resultant electronic states of this material can be fine-tuned from the Dirac-cone-dominating state (KNi_4S_2, x = 1) to the flat-band-dominating state ($K_0Ni_4S_2$, x = 0). In addition, a non-Fermi liquid behavior with a universal linear-temperature-dependent electrical resistivity is observed across all K-levels, suggesting the strange metal behavior. Such non-Fermi liquid behavior is often associated with emerging collective excitations near a quantum critical point, as seen in high-T_c cuprates,[56] iron-based superconductors,[57] and heavy-fermion metals.[12,14,58] Similarly, such linear or sublinear transports are also widely observed in Kagome metal

Please cite this article in press as: Zhao et al., Evolution from topological Dirac metal to flat-band-induced antiferromagnet in layered $K_xNi_4S_2$ ($0 \leq x \leq 1$), Matter (2025), https://doi.org/10.1016/j.matt.2025.102418

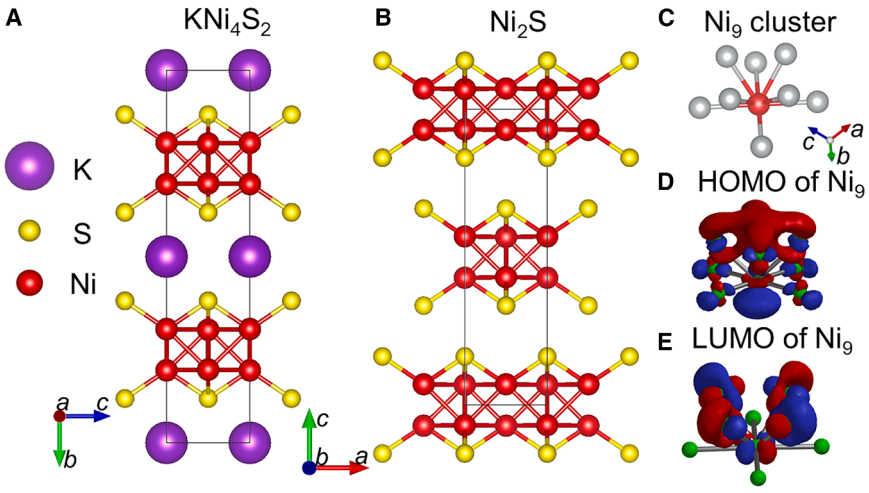

Figure 1. Crystal structures and origin of Dirac cones

(A and B) Crystal structures of KNi_4S_2 (x = 1, space group *Cmmm*) (A) and Ni_2S (x = 0, space group *Cmcm*) (B). The atoms of K, Ni, and S are depicted in purple, red, and yellow, respectively.

(C–E) A Ni_9 cluster with red for the center Ni atom and gray for the surrounding Ni atoms (C), highlighting the Ni–Ni bonding in $K_xNi_4S_2$ and the molecular orbitals of its highest occupied molecular orbital (HOMO) (D) and lowest occupied molecular orbital (LUMO) (E). Note that the red and blue colors denote + and – signs of MO, respectively.

systems,[59] which can be described by a semiclassical two-pocket model, highlighting the interplay between fast electrons from Dirac cones and weak dispersive electrons from flat bands or VHSs.[60] Therefore, the presence of strange metal behavior indicates that strong correlations between the Dirac cones and flat bands are present across the whole series of $K_xNi_4S_2$ ($0 \leq x \leq 1$), whose ground state alternates between a non-magnetic Dirac metal on the x = 1 side and a flat-band-induced antiferromagnetic (AFM) metal on the x = 0 side through the K-deintercalation process.

RESULTS AND DISCUSSION

Origin of coexisting Dirac cones and flat bands

KNi_4S_2 (x = 1) crystallizes in the $CeRe_4Si_2$ type[61] with space group *Cmmm* (Tables S1 and S2), featuring two Ni sheets sandwiched between two S sheets (Figure 1A) and unconventionally low formal oxidation states for nickel of $Ni^{0.75+}$. The potassium atoms in KNi_4S_2 can be deintercalated topotactically in various degrees until the formation of the completely K-free Ni_2S (x = 0)[53] with a formal oxidation state of Ni^{1+}. Ni_2S crystallizes in the space group *Cmcm*, exhibiting the same structural features of KNi_4S_2 but with van der Waals gaps between the layers (Figure 1B). There are extensive Ni–Ni bonds in the structure because of the low valent electron-rich character on these atoms. Consequently, certain Ni atoms can be bonded to nine other Ni atoms to form a Ni_9 cluster. (Figure 1C)

To gain deeper insights into such Ni–Ni bonding and its implications, we performed density functional theory (DFT) calculations on an isolated Ni_9 cluster (Figure 1C). Its highest occupied molecular orbital (HOMO) (Figure 1D) shows a strong Ni-d_{z^2} character at the center and $d_{x^2-y^2}$ for the surrounding Ni. Conversely, the lowest unoccupied molecular orbital (LUMO) (Figure 1E) reveals the opposite trend, showing strong Ni-$d_{x^2-y^2}$ character at the center and d_{z^2} for the surrounding Ni. The protruding d_{z^2} orbitals perpendicular to the square net resemble the p_z orbitals in graphene, which is essential for the creation of Dirac cones in the honeycomb lattice. A two-band symmetry analysis for the square lattice also suggested the possible formation of Dirac cones using an $s/d_{x^2-y^2}$ model,[54] where the *s* band can be replaced by d_{z^2} for the same a_{1g} symmetry. This bonding analysis suggests pivotal roles played by the unique Ni–Ni interactions in the formation of Dirac cones hosted by the $K_xNi_4S_2$ system.

Tuning the Fermi level through topochemical K-deintercalation

Electronic band structure calculations were performed for $K_xNi_4S_2$ ($0 \leq x \leq 1$) with different K-deintercalation levels (Figure 2; see details in supplemental information). Two main features are noteworthy across the whole series. The first remarkable feature is the presence of Dirac cones, a signature of topological materials,[28–31] from Γ-X and Z-A points above the Fermi level. The Fermi level sits right below Dirac cones for x = 1 (Figure 2A, E_{Dirac} = 25 meV for x = 1) and gradually shifts away with reduced degeneracy as the K-deintercalation proceeds (Figures 2B and 2C, E_{Dirac} = 259 meV for x = 0). The splitting of the Dirac cone along Γ-X for the x = 0 compound is likely a result of the unit cell change caused by the shifting of the Ni_4S_2 layers induced by the K-deintercalation[53]; however, it is interesting that the Dirac cone degeneracy remains the same along Z-A, suggesting a different local electronic environment between the two Ni–Ni square-net layers.

Besides Dirac cones, another interesting characteristic of the electronic structure involves multiple flat bands below the Fermi level near the M-point along X-M-Γ. Opposite to the evolution of Dirac cones, the Fermi level resides distantly above flat bands for the x = 1 compound (Figure 2A, $E_{flat} = -239$ meV for x = 1), and the K-deintercalation progressively shifts the Fermi level toward flat bands (Figures 2B and 2C, $E_{flat} = -82$ meV for x = 0). The shift of the Fermi level upon K-deintercalation is corroborated by the work function measurement along with the discovery of largely enhanced interlayer interactions between adjacent Ni_2S layers during the K-deintercalation (Figures S1 and S2).

Further topological invariant analysis, including the Wannier charge center calculations (Figure S3), confirms the nontrivial Z_2 invariant of KNi_4S_2 (x = 1). The Z_2 number at all k_i = 0.0 (i = 1,2,3 for x,y,z) planes is 1, whereas that at k_i = 0.5 (i = x,y,z) planes is 0. These findings indicate that KNi_4S_2 (x = 1) is a strong topological material with a Z_2 index of 1;(000) according to the Fu-Kane classification,[62] similar to that of Bi_2Se_3.[63] Combined

Please cite this article in press as: Zhao et al., Evolution from topological Dirac metal to flat-band-induced antiferromagnet in layered $K_xNi_4S_2$ ($0 \leq x \leq 1$), Matter (2025), https://doi.org/10.1016/j.matt.2025.102418

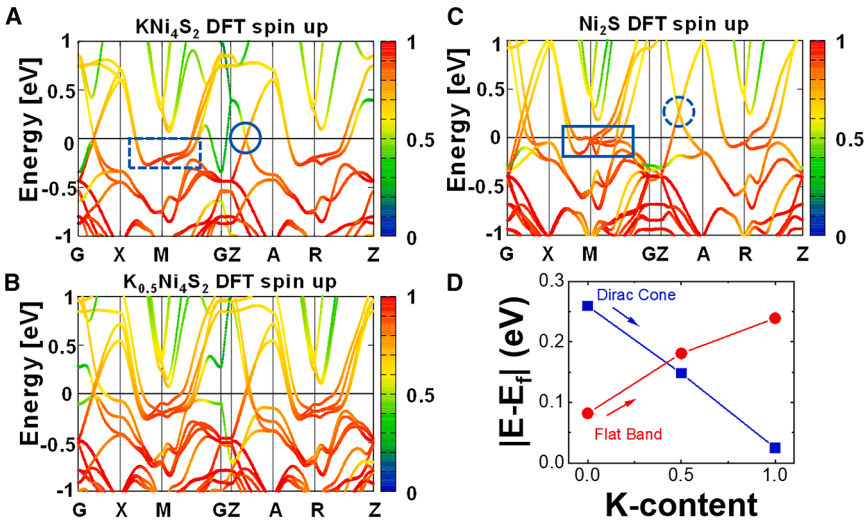

Figure 2. Evolution of ground states revealed from electronic band structure calculations

(A) Density functional theory calculations of $K_xNi_4S_2$ with band structures showing projections of Ni *3d* electrons for KNi_4S_2 (x = 1). Note: Dirac cones are visible at the Fermi level between the G-X and Z-A points.

(B and C) $K_{0.5}Ni_4S_2$ (x = 0.5) (B) and Ni_2S (x = 0) (C). The scale on the right side of each image illustrates the fractional contributions of Ni *3d* electrons. Flat bands are visible near the Fermi level at the M point; note that the flat bands and Dirac cones are highlighted with a square and circle, respectively, with solid lines indicating proximity to the Fermi surface and dashed lines representing distance from the Fermi surface.

(D) A summary of $|E-E_f|$ as a function of K-content for the Dirac cone and flat-band features.

with the observed band inversion near the Fermi level, KNi_4S_2 (x = 1) is expected to be a topologically nontrivial Dirac metal. In contrast, a trivial electronic structure is observed for the fully deintercalated Ni_2S (x = 0), both in non-magnetic and AFM spin configurations, with a trivial Z_2 index of 0;(000). The band inversion is also observed in the non-magnetic configuration of Ni_2S (x = 0); however, the inverted band is far away from the Fermi level, which results in trivial band topology (Figure S4). Interestingly, such band inversion vanishes with the presence of an AFM order, signifying that the topological feature in $K_xNi_4S_2$ may emerge as a synergistic consequence of magnetic order and charge carrier adjustments into the Ni_4S_2 layers from K-deintercalation.

In essence, our first-principles calculations (Figure 2D) predict a tunable ground state of $K_xNi_4S_2$ with the Dirac-cone-dominating state on the x = 1 (KNi_4S_2) side, extending toward the flat-band-dominating state on the fully K-intercalated x = 0 (Ni_2S) side. In the following section, we provide our experimental evidence to showcase the rich and tunable ground states of $K_xNi_4S_2$ ($0 \leq x \leq 1$).

Topological Dirac metal

A linearly temperature-dependent resistivity is observed across all $K_xNi_4S_2$ compositions (Figure 3A), despite approaching the Ioffe-Regel limit upon K-deintercalation,[64] suggesting the strange metal behavior. The persistence of such non-Fermi liquid behavior highlights the underlying strong correlations across the $K_xNi_4S_2$ system[12,52,56,65,66] and the interplay between Dirac cones and flat bands.[60] In the following, we begin by examining the K-rich region, which projects the physical properties induced by the Dirac cones.

A signature of Dirac metals is the linearly dispersed band near the Fermi level, leading to the high mobility of charge carriers. To explore such characteristics, we performed magnetoresistance (defined as MR = $[\rho(H) - \rho(0)]/\rho(0) \times 100\%$) utilizing a horizontal rotator with the magnetic field rotating between the out-of-plane ($\theta = 90°$) and in-plane ($\theta = 0°$) directions, relative to the Ni_2S plane of the single crystal under investigation. A single crystal with a high K-content of x = 0.7 was first measured. The anisotropic MR aligns with the low-dimensional nature of the system (Figure 3B), whereas the large MR suggests the existence of high-mobility charge carriers near the Fermi surface. It is worth mentioning that non-saturating linear MR (Figures 3C and S7C) bears similarities to many high-T_c cuprates, and its coexistence with the strange metal behavior (Figure 3A) further highlights the presence of strong correlations.[56]

To demonstrate the shift of the Fermi level away from Dirac cones induced by the K-deintercalation, we performed similar measurements on another single crystal with fully deintercalated K-content (x = 0). The diminishing MR of the x = 0 compound confirms a significantly reduced carrier mobility due to the shifting away of Dirac cones (Figures 3C and S8). As suggested by the Hall effect data, electrons are the dominant carriers across the whole series of $K_xNi_4S_2$ (Figures 3D and S9), with the x = 0 compound showing a 2-fold enhancement of carrier density compared to the x = 0.7 compound (Figure 3E), likely originating from flat bands near the Fermi surface. Extracted from the Hall effect data, a quantitative comparison shows that an order-of-magnitude carrier mobility reduction from μ (x = 0.7) = 1,471 $cm^2V^{-1}s^{-1}$ down to μ (x = 0) = 9.4 $cm^2V^{-1}s^{-1}$ at 1.8 K can be achieved through the K-deintercalation process (Figures 3F and S10), which is consistent with the DFT prediction discussed previously (Figure 2). The electrical transport results support the first-principles predictions that the Fermi level shifts away from Dirac cones as the K-deintercalation process proceeds.

We now focus on the emergence of the flat band near the Fermi level as the system approaches the more K-deintercalated region, starting with the heat capacity results, followed by flat-band magnetism.

Flat-band-induced magnetism

The low-temperature heat capacity of $K_xNi_4S_2$ can be well described by $C(T) = \gamma T + \beta T^3$, where γ and β are the Sommerfeld

Please cite this article in press as: Zhao et al., Evolution from topological Dirac metal to flat-band-induced antiferromagnet in layered $K_xNi_4S_2$ ($0 \leq x \leq 1$), Matter (2025), https://doi.org/10.1016/j.matt.2025.102418

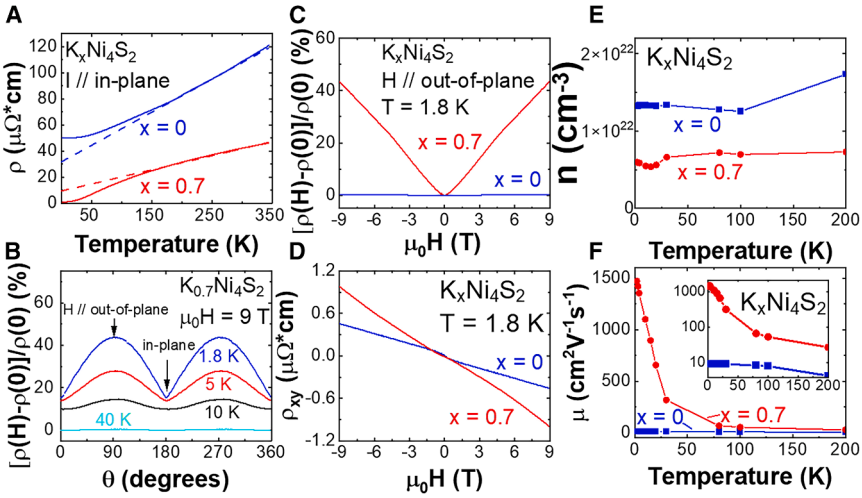

Figure 3. Dirac-cones-dominating states

(A–F) The electrical transport of $K_xNi_4S_2$, with temperature-dependent in-plane electrical resistivity (A); angular-dependent magnetoresistance of $K_{0.7}Ni_4S_2$ with 9 T of magnetic field (B); comparisons of magnetoresistance (C) and Hall effect (D) at 1.8 K between x = 0.7 and x = 0; and the extracted carrier density (E) and carrier mobility (F) as a function of temperature. The inset of (F) shows the carrier mobility on a log scale.

coefficient and Debye constant, respectively (Figures 4A and 4B). The Sommerfeld coefficient, γ, represents the electronic contribution. The flatness of the electronic bands near the Fermi surface can be evaluated through γ, as a large value of γ typically suggests enhanced electronic correlations, for example, due to the flat band classically seen in the heavy fermion systems.[11] As expected, a more than 2-fold enhancement of γ is observed as the K-deintercalation process proceeds, increasing from γ = 32.9 mJ/mol/K^2 for x = 1 to γ = 57.92 mJ/mol/K^2 for x = 0.7 first and eventually to γ = 75.99 mJ/mol/K^2 for x = 0 (Figure 4C). Although a large value of γ is observed across the whole $K_xNi_4S_2$ system, the Kadowaki-Woods ratio analysis suggests that $K_xNi_4S_2$ is a *d*-band metal instead of a heavy fermion material (Note S2; Figure S6). Nevertheless, the enhanced electronic correlations suggested by the γ values corroborate the first-principles predictions that the Fermi level moves toward flat bands as the K-deintercalation process proceeds (Figure 2D).

The enhanced electronic correlations originating from flat bands can favor electronic instabilities, such as ferromagnetism, known as Stoner's criterion for ferromagnetism.[7] Accordingly, an emerging AFM transition below 10 K gradually develops as the K-deintercalation proceeds in $K_xNi_4S_2$ (Figures 4D–4G and S11). However, both the anomalously large temperature-independent term χ_0 (Figures S11A and S11B) and the existence of ferromagnetic (FM)-like signals from isothermal magnetization,

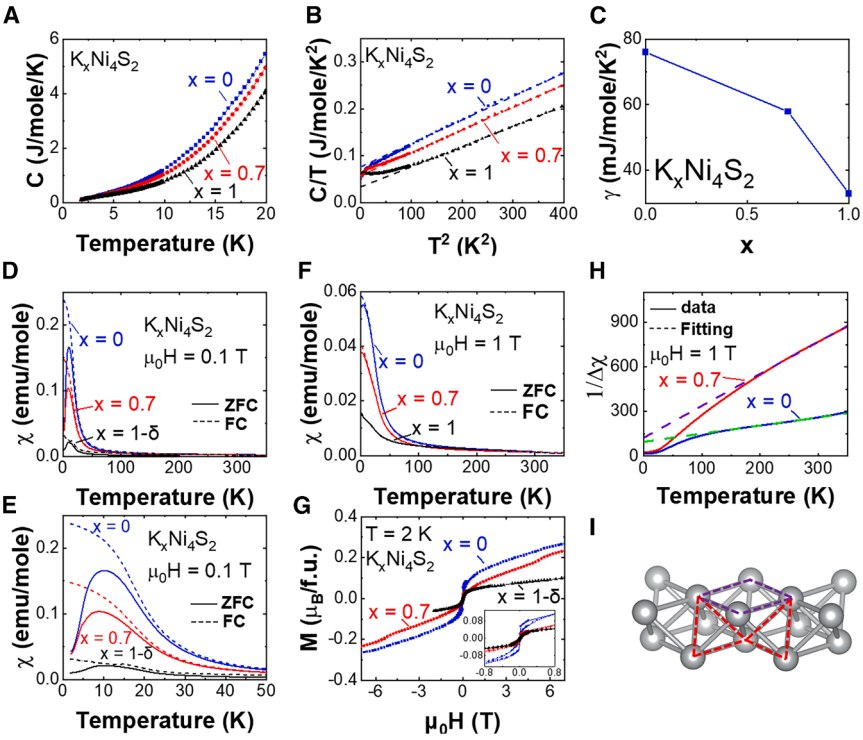

Figure 4. Flat-bands-dominating properties

(A–I) Heat capacity and magnetic susceptibility measurements of $K_xNi_4S_2$, with C vs. T (A) and C/T vs. T^2 (B) for x = 0, 0.7, and 1; the extracted Sommerfeld coefficient γ (C). Magnetic susceptibility with 0.1 T magnetic field following field-cooling (FC) and zero-FC (ZFC) protocols (D); a zoomed-in view at low-temperature region (E); with 1 T magnetic field (F); isothermal magnetization at T = 2 K (G) with a zoomed-in view in the inset; the $1/\Delta\chi$ and the Curie-Weiss fitting (H); and a schematic showing the local triangular (red dashed lines) and square (purple dashed lines) geometry of Ni that potentially leads to the observed spin frustrations (I).

apparent even well above the Néel temperature (T_N) (Figure S11C), suggest the presence of small FM impurities with high T_c. Such impurity is attributed to metallic Ni that forms in the strong basic synthesis environment.[53] Among all the samples characterized, the x = 0.7 sample shows the least, if not the absence of, FM impurity; thus, we use x = 0.7 as the baseline to normalize the rest of the data by a constant χ_0. A detailed discussion regarding the removal of the FM impurity signal is included in Note S4.

After correcting for the impurity contribution, it is clear that an AFM order gradually develops upon K-deintercalation (Figure 4D), with a varying T_N raised from 8.6 K for x = 0.7 to 10.1 K for x = 0 (Figure 4E). A transition is also observed in x = 1 with a T_N of ~10 K. The substantially weaker signal observed in the x = 1 specimen originates from minor K-deintercalated phases formed during the sample washing process. Therefore, we label it as $x = 1 - \delta$. To test this interpretation, we conducted neutron powder diffraction (NPD) measurements on the x = 1 sample and observed no additional magnetic reflections between 260 and 5 K, confirming the absence of long-range magnetic order (Figure S12). A weak magnetic hysteresis also gradually develops upon K-deintercalation (Figure 4G, inset), suggesting a canted AFM order. However, no spin saturation is observed up to 7 T (Figure 4G). The canted-AFM nature is further evidenced by the splitting of the magnetic susceptibility between the field-cooling (FC) and zero-FC (ZFC) measurements, as well as the suppressed T_N with increasing magnetic field (Figures 4E, 4F, and S13). Alternatively, the bifurcation of FC and ZFC data may also be attributed to the spin glass state, as the heat capacity reveals no clear second-order phase transition across the T_N (Figure 4A). Hence, to clarify the magnetic ground state further, we carried out alternating-current (AC) magnetic susceptibility at varying frequencies between 1 and 1,000 Hz on the x = 0 compound. The lack of any frequency-dependent shift in either of the real (χ', Figure S14A) or imaginary (χ'', Figure S14B) components across the T_N suggests the absence of spin-glass behavior. In addition, first-principles calculations also suggest competing FM and AFM configurations are present on the x = 1 side, which could be another reason for the absence of magnetic order in KNi_4S_2. On the contrary, only one AFM configuration is preferred for the fully deintercalated x = 0 compound (Figure S15).

For the Curie-Weiss analysis, we applied a strong magnetic field of 1 T to fully saturate the FM impurity contribution, which was treated as a temperature-independent term, χ_0. The inverse magnetic susceptibility above 200 K follows the Curie-Weiss law (Figure 4H), yielding a Curie-Weiss temperature, θ_{CW}, and an effective moment, μ_{eff}, of −57.4 K and 0.49 μ_B/Ni and −177.7 K and 0.96 μ_B/Ni for x = 0.7 and x = 0, respectively. The estimated effective moment is enhanced 2-fold as the K-deintercalation proceeds. The effective moment is intermediate between Ni^{1+} (1.73 μ_B/Ni) and Ni^0, consistent with the electron-rich nature of $K_xNi_4S_2$, where the averaged valence state of Ni ranges from $Ni^{0.75+}$ (x = 1) to Ni^{1+} (x = 0). The large negative θ_{CW} indicates strong AFM interactions, consistent with the material's AFM ground state. Furthermore, the resultant frustration parameter ($f = |\theta_{CW}|/T_N$) enhanced from 6.7 to 17.6 as the K-deintercalation level decreased from x = 0.7 to x = 0, indicating enhanced magnetic frustration[67] despite the precipitation of a magnetic order. The observed spin frustration may be attributed to the presence of local triangular geometry (red dashed line in Figure 4I). In addition to the well-known geometric frustration associated with triangular geometry, frustration can also occur in square lattices (purple dashed line in Figure 4I) when second-nearest-neighbor magnetic interactions dominate over those between nearest neighbors, a scenario observed in many Fe-based superconductors.[68–70] Interestingly, the coexistence of spin frustration, strange metal behavior, and a flat-band-dominating Fermi surface closely parallels the characteristics of another Kagome system, Ni_3In.[52]

In addition to flat-band-induced magnetism, the enhanced electron correlations may also lead to flat-band superconductivity, as discovered recently in twisted bilayer graphene.[1–4] Furthermore, the strange metal behavior and linear MR of $K_xNi_4S_2$ (Figure 3) also resemble high-T_c cuprates.[56] However, we observed no evidence of superconductivity down to 3.4 K under 10 GPa of hydrostatic pressure (Figure S16). Instead, pressure-induced lattice distortions, as indicated by a reduced residual-resistance ratio and orthorhombic distortions (Figures S16A and S16B), likely dominate the observed physical properties.

Conclusions

The $K_xNi_4S_2$ ($0 \leq x \leq 1$) simultaneously hosts both flat bands and Dirac cones at two different energies that can be accessed with intercalation/deintercalation processes and represents a unique case of a system lacking the Kagome or honeycomb lattice. The flexibility of hosting a wide range of K-content in its structure enables a change of the Fermi level over a wide range of energy. Notably, the ground state of $K_xNi_4S_2$ ($0 \leq x \leq 1$) can be fine-tuned from a non-magnetic topological Dirac metal (KNi_4S_2, x = 1) to a flat-band-containing AFM metal (Ni_2S, x = 0) through a deintercalation process. In addition, our *ex situ* topochemical K-deintercalation work demonstrates the feasibility for the potential *in situ* control of quantum materials between a Dirac-cone-dominating state, a flat-band-dominating state, and intermediate states by, for instance, electrochemically tuning the K-intercalation levels to move the Fermi energy.[71] This unique capability provides a platform for exploring fundamental physical phenomena and creates opportunities for applications, including reconfigurable electronics, multi-state memory devices, and adaptive sensors, where dynamic control of electronic properties is necessary.

METHODS

Synthesis

For the synthesis of KNi_4S_2, $Ni(OH)_2$ and S were ground with a hydroxide flux consisting of a mixture of LiOH and KOH with the molar ratio of n(LiOH)/n(KOH) = 0.55/0.45 using a methodology described earlier.[72,73] The molar ratio of $Ni(OH)_2$:S was kept constant at about 1:2.5 to ensure an excess amount of S for the Ni source. Once all the starting materials were thoroughly mixed, they were loaded into a glassy carbon crucible and then placed in a quartz tube. The quartz tube was placed in a tube furnace horizontally with both ends connecting to O-ring-sealed metal flanges that allowed an inert gas, such as N_2, to pass through during the reaction. The furnace was heated to 450°C at a rate

of 5°C/min, then kept at 450°C for 20–30 h, and then cooled to room temperature (RT) at a rate of 7°C–50°C/h (cooling rate appeared not to affect the product). After the furnace was cooled to RT, the reaction vessel was immersed in a beaker filled with water and then ultrasonicated until all hydroxides were dissolved. The ternary K-Ni-S products were obtained by decantation of the solution and subsequent washing with methanol and drying in air. We found two methods for controllable K-deintercalation: (1) using a flux composition that favors a Ni oxidation state higher than $Ni^{0.75+}$ and (2) synthesizing the KNi_4S_2 first and soaking KNi_4S_2 crystals with hydroxide fluxes in methanol. We found that the K-deintercalation level is more homogeneous and controllable using the second method. The level of K-deintercalation was controlled by soaking time while washing the residual hydroxide flux with methanol. All ternary products appeared to be stable in the air for up to a few days. Crystals up to 1 mm in length could be obtained and used for subsequent structural determination and physical properties characterization.

X-ray and neutron diffraction at ambient pressure

Powder X-ray diffraction (PXRD) data were collected using a Rigaku Miniflex X-ray diffractometer with Cu K_α radiation, λ = 1.5418 Å. Temperature-dependent single-crystal XRD (SXRD) data between 100 and 300 K were collected using a synchrotron X-ray with λ = 0.41328 Å at 15-IDD at the Advanced Photon Source (APS). NPD measurements were performed using the BT-1 high-resolution neutron powder diffractometer at the NIST Center for Neutron Research with the Ge (311) monochromator (λ = 2.0772 Å) and the 60′ in-pile collimator. In addition to base temperature measurement (~4 K), data at 25 and 260 K were also collected to investigate possible structural or magnetic transitions.

DC magnetic susceptibility

Direct-current (DC) magnetic susceptibility (χ_{dc}) data for coaligned single crystals were collected with a magnetic property measurement system (MPMS3, Quantum Design). Temperature-dependent magnetic measurements were performed from 2 to 300 K in both FC and ZFC conditions, while field-dependent data were collected under applied fields of up to 7 T.

AC magnetic susceptibility

AC magnetic susceptibility (χ_{ac}) was measured with a 14 T Quantum Design physical property measurement system (PPMS-14) on powder samples. ZFC measurements were taken from 40 to 1.8 K with varying AC-frequencies from 1 to 1,000 Hz.

Electrical resistivity, Hall effect, and heat capacity measurements

Electrical resistivity with the standard four-probe method and Hall effect with standard four-probe Hall configuration were performed with a single crystal of $K_xNi_4S_2$ using 9 T Dynacool quantum design physical property measurement system (PPMS-Dynacool) equipment with a horizontal rotator. Heat capacity measurements of coaligned single crystals of $K_xNi_4S_2$ were carried out on a physical property measurement system (PPMS-Dynacool).

Theoretical methods

We adopted the DFT calculation to compute the band structure and the Fermi surface of KNi_4S_2, $K_{0.5}Ni_4S_2$, and Ni_2S using the Vienna Ab initio Simulation Package (VASP).[74,75] The Perdew-Burke-Ernzerhof for solids (PBE-sol)[76] implementation was used as the exchange-correlation functional within DFT. The gamma-centered Monkhorst-Pack *k*-point mesh of 8 × 8 × 2 and the plane-wave energy cutoff of 400 eV were used for both materials. MO calculations were performed using Spartan'24 with a range-separated hybrid generalized gradient approximation (RSH-GGA) ωB97X-D as the functionals.[77] The electronic structure topological analysis was performed using WannierTools.[78] The Wannier basis and Hamiltonian were constructed using Wannier90[79] based on DFT calculations using the VASP.[74,75] The band structure and DOS were also computed using the VASP. The projector augmented-wave method and plane-wave basis were employed for electron orbitals, charge density, and electron-nuclei interactions with a cutoff energy of 400 eV.[80] Hubbard *U* corrections for Ni *d* orbitals were added in the electronic structure topological analysis to describe the orbital localization with U = 5 eV properly. Noncollinear magnetization with spin-orbit couplings was considered within the GGA and PBE functional.[81]

Electrical transport properties under high pressure

Electrical transport measurements of KNi_4S_2 bulk single crystals were conducted using the quasi-four-terminal method with NaCl as the pressure-transmitting medium (PTM). All the measurements were carried out in a diamond anvil cell (DAC) with a 500 μm culet size. The gasket was prepared from a 250-μm-thick stainless-steel sheet, which was pre-indented to a thickness of approximately 60 μm. For all measurements, an initial hole of ~150 μm in diameter was created. The indented gasket was then insulated using a fine alumina and epoxy mixture. After insulation, a ~120 μm hole was laser drilled through the compressed gasket. Fine NaCl powder was loaded into the hole, and the pressure was gradually increased to ~2.0 GPa until the NaCl turned transparent. Then, a rectangular plate-like KNi_4S_2 single crystal was carefully loaded on top of the transparent NaCl, and four platinum electrodes were arranged to contact the sample. The temperature-dependent resistance of KNi_4S_2 was measured in a closed-cycle cryocooler system (2.4–300 K) using a Stanford Research SR830 digital lock-in amplifier with a current of 100–1,000 μA. Pressure was measured using the ruby fluorescence method,[82] both at RT and a low temperature of ~4.2 K, with the aid of an online ruby system.

PXRD under high pressure

High-pressure XRD measurements were conducted using a symmetric DAC with 500 μm culet Boehler-type diamonds and a stainless-steel gasket. Pressure was determined using both ruby fluorescence[83] and the equation of state (EoS) of gold (Au), with measurements taken before and after each diffraction scan to ensure accuracy. A KNi_4S_2 powder sample, approximately 25 × 25 × 10 μm^3 in size, was loaded into the DAC, with neon used as the PTM. XRD data were collected up to 20.2 GPa. The X-ray experiments were performed at beamline 16-BM-D of the High Pressure Collaborative Access Team

(HPCAT) at the APS, Argonne National Laboratory (ANL), using an X-ray with a wavelength of $\lambda = 0.4066$ Å. Diffraction images were collected in angle-dispersive geometry while rotating the DAC by approximately 50°, enabling comprehensive capture of the Bragg peaks. The 2D images were integrated using the Dioptas program,[84] and the resulting powder patterns were analyzed by Le Bail fitting using the GSAS-EXPGUI package.[85] Single-crystal X-ray structures of KNi_4S_2 were used as starting models for the refinement of all the powder data. Although data quality declined above 12.2 GPa, the position of the diffraction peaks indicated no structural phase transition up to the maximum pressure measured (20.2 GPa). Moreover, the least-squares fitting of pressure-volume data from the third-order Birch-Murnaghan EoS was performed with the aid of EoSFit7c software.[86]

SEM/transmission electron microscope characterization

Microscopic images were examined on a Hitachi SU-70 SEM field-emission scanning electron microscope (SEM), and their elemental compositions were determined by energy-dispersive X-ray spectroscopy (EDS) using a BRUKER EDS detector.

Photoemission yield spectroscopy in air

Photoemission yield spectroscopy in air (PYSA) was measured using a Riken-Keiki AC-2 instrument equipped with a tunable monochromatic ultraviolet (UV) light source that produces light in the 4.2–7 eV range. The $K_xNi_4S_2$ (x = 0, 0.7, 1) materials were scanned in the 4.2–6.2 eV range, with the generated photoelectrons being measured at each energy step. $K_0Ni_4S_2$ (x = 0) was measured using a 0.05 eV step size and a 20-s counting time with a UV intensity of 100 nW. The data for $K_{0.7}Ni_4S_2$ (x = 0.7) and KNi_4S_2 (x = 1) were collected using a 0.1 eV step size and a 10-s counting time with a UV intensity of 800 nW. For all samples, a quantity of light correction was utilized over the measured energy range to account for fluctuations in the UV lamp's intensity. The square root of the photoelectron counts per second was plotted vs. the energy of the incident light, and the work function of each sample was determined through the intersection of the regression lines from the baseline and linear onset of the obtained PYSA data. The negative of the work function value provides information on the position of the Fermi level of the material relative to the free electron.

RESOURCE AVAILABILITY

Lead contact

Requests for further information and resources should be directed to and will be fulfilled by the lead contact, Mercouri G. Kanatzidis (m-kanatzidis@northwestern.edu).

Materials availability

The materials generated in this study may be made available upon request.

Data and code availability

- All data reported in this paper, such as those in the methods section, and additional physical property characterizations, such as magnetotransport, heat capacity, magnetic susceptibility measurements, and PYSA, will be shared by the lead contact upon request.
- This paper does not report original code.
- Crystallography data have been deposited at the Cambridge Crystallographic Data Center under the database identifiers CCDC: 2088104–2088106 and are publicly available as of the date of publication.

ACKNOWLEDGMENTS

This work is primarily supported by the US Department of Energy (DOE), Office of Science, Basic Energy Sciences, Materials Sciences and Engineering Division. This material is based upon work supported by Laboratory Directed Research and Development funding from ANL, provided by the Director, Office of Science, of the US DOE under contract no. DE-AC02-06CH11357. The work (SEM/EDX) performed at the Center for Nanoscale Materials, a US DOE Office of Science User Facility, was supported by the US DOE, Office of Basic Energy Sciences, under contract no. DE-AC02-06CH11357. Work at the beamline 15-IDD at the APS at ANL was supported by the US DOE, Office of Science, Office of Basic Energy Sciences, under contract no. DE-AC02-06CH11357. The National Science Foundation (NSF)'s ChemMatCARS Sector 15 is supported by the Divisions of Chemistry (CHE) and Materials Research (DMR), NSF, under grant no. NSF/CHE-1834750 and NSF/CHE-2335833. X.Z. acknowledges support from the Georgetown University startup fund. T.D. acknowledges the computational resources provided by the National Supercomputer Center in Tianjin. H.P. acknowledges the computing resources provided by Bebop, a high-performance computing cluster operated by the Laboratory Computing Resource Center at ANL. The research at the University of Utah is supported by NSF Division of Materials Research award no. 2132692, as well as the US DOE Office of Science Fusion Energy Sciences funding award entitled High Energy Density Quantum Matter, award no. DE-SC0020340. R.K. and R.H. acknowledge support from DOE-NNSA (DE-NA0003975) through the Chicago/DOE Alliance Center and DOE-SC (DE-SC0020340). HPCAT operations are supported by the DOE-NNSA Office of Experimental Sciences. The APS is a DOE Office of Science User Facility operated for the DOE, Office of Science, by ANL under contract no. DE-AC02-06CH11357.

AUTHOR CONTRIBUTIONS

The work was conceived by H.Z., X.Z., D.-Y.C., and M.G.K., with input from all authors. H.Z. carried out the synthesis, XRD, electrical transport, heat capacity, DC magnetic susceptibility measurements, data analysis, and writing. X.Z. carried out the powder neutron diffraction, synchrotron XRD, MO bonding analysis, and writing. H.P. performed first-principles electronic band structure calculations. T.D. analyzed topological properties and contributed to writing. B.W. performed AC magnetic susceptibility measurements. C.M.B. and H. W. conducted powder neutron diffraction measurements. S.E.P. and Z.-L.X. contributed to magnetotransport data analysis. T.B. performed high-pressure transport measurements and high-pressure XRD analysis. T.M. performed high-pressure transport measurements. W.C. analyzed high-pressure XRD results. R.K. collected and analyzed high-pressure XRD results. S.D. performed high-pressure electrical resistivity measurements. R.H. contributed to high-pressure powder diffraction measurements. A.P.A. II conducted and analyzed PYSA measurements. Y.-S.C. collected synchrotron XRD data. S.R., D.-Y.C., and M.G.K. supervised the project.

DECLARATION OF INTERESTS

The authors declare no competing interests.

SUPPLEMENTAL INFORMATION

Supplemental information can be found online at https://doi.org/10.1016/j.matt.2025.102418.

Received: May 23, 2025
Revised: July 4, 2025
Accepted: August 12, 2025

REFERENCES

1. Cao, Y., Rodan-Legrain, D., Rubies-Bigorda, O., Park, J.M., Watanabe, K., Taniguchi, T., and Jarillo-Herrero, P. (2020). Tunable correlated states and spin-polarized phases in twisted bilayer–bilayer graphene. Nature *583*, 215–220.
2. Cao, Y., Fatemi, V., Demir, A., Fang, S., Tomarken, S.L., Luo, J.Y., Sanchez-Yamagishi, J.D., Watanabe, K., Taniguchi, T., Kaxiras, E., et al. (2018). Correlated insulator behaviour at half-filling in magic-angle graphene superlattices. Nature *556*, 80–84.
3. Lisi, S., Lu, X., Benschop, T., de Jong, T.A., Stepanov, P., Duran, J.R., Margot, F., Cucchi, I., Cappelli, E., Hunter, A., et al. (2021). Observation of flat bands in twisted bilayer graphene. Nat. Phys. *17*, 189–193.
4. Tian, H., Gao, X., Zhang, Y., Che, S., Xu, T., Cheung, P., Watanabe, K., Taniguchi, T., Randeria, M., Zhang, F., et al. (2023). Evidence for Dirac flat band superconductivity enabled by quantum geometry. Nature *614*, 440–444.
5. Li, Y., Yin, Z., Liu, Z., Wang, W., Xu, Z., Song, Y., Tian, L., Huang, Y., Shen, D., Abernathy, D.L., et al. (2019). Coexistence of Ferromagnetic and Stripe Antiferromagnetic Spin Fluctuations in $SrCo_2As_2$. Phys. Rev. Lett. *122*, 117204.
6. Liu, Z.H., Zhao, Y.G., Li, Y., Jia, L.L., Cai, Y.P., Zhou, S., Xia, T.L., Büchner, B., Borisenko, S.V., and Wang, S.C. (2015). Orbital characters and electronic correlations in KCo_2Se_2. J. Phys. Condens. Matter *27*, 295501.
7. Stoner, E.C. (1938). Collective electron ferromagnetism. Proceedings of the Royal Society of London. Series A. Mathematical and Physical Sciences *165*, 372–414.
8. Huang, J., Wang, Z., Pang, H., Wu, H., Cao, H., Mo, S.-K., Rustagi, A., Kemper, A.F., Wang, M., Yi, M., and Birgeneau, R.J. (2021). Flat-band-induced itinerant ferromagnetism in $RbCo_2Se_2$. Phys. Rev. B *103*, 165105.
9. Kitaori, A., Kanazawa, N., Yokouchi, T., Kagawa, F., Nagaosa, N., and Tokura, Y. (2021). Emergent electromagnetic induction beyond room temperature. Proc. Natl. Acad. Sci. USA *118*, e2105422118.
10. Yang, J., Chen, B., Wang, H., Mao, Q., Imai, M., Yoshimura, K., and Fang, M. (2013). Magnetic properties in layered ACo_2Se_2 (A=K, Rb, Cs) with the $ThCr_2Si_2$-type structure. Phys. Rev. B *88*, 064406. https://doi.org/10.1103/PhysRevB.88.064406.
11. Stewart, G.R. (1984). Heavy-fermion systems. Rev. Mod. Phys. *56*, 755–787. https://doi.org/10.1103/RevModPhys.56.755.
12. Checkelsky, J.G., Bernevig, B.A., Coleman, P., Si, Q., and Paschen, S. (2024). Flat bands, strange metals and the Kondo effect. Nat. Rev. Mater. *9*, 509–526.
13. Kirchner, S., Paschen, S., Chen, Q., Wirth, S., Feng, D., Thompson, J.D., and Si, Q. (2020). Colloquium: Heavy-electron quantum criticality and single-particle spectroscopy. Rev. Mod. Phys. *92*, 011002.
14. Paschen, S., and Si, Q. (2020). Quantum phases driven by strong correlations. Nat. Rev. Phys. *3*, 9–26.
15. Teng, X., Chen, L., Ye, F., Rosenberg, E., Liu, Z., Yin, J.-X., Jiang, Y.-X., Oh, J.S., Hasan, M.Z., Neubauer, K.J., et al. (2022). Discovery of charge density wave in a kagome lattice antiferromagnet. Nature *609*, 490–495.
16. Lu, Z., Han, T., Yao, Y., Reddy, A.P., Yang, J., Seo, J., Watanabe, K., Taniguchi, T., Fu, L., and Ju, L. (2024). Fractional quantum anomalous Hall effect in multilayer graphene. Nature *626*, 759–764.
17. Terada, T., Uematsu, Y., Ishibe, T., Naruse, N., Sato, K., Nguyen, T.Q., Kobayashi, E., Nakano, H., and Nakamura, Y. (2022). Giant enhancement of seebeck coefficient by deformation of silicene buckled structure in calcium-intercalated layered silicene film. Adv. Mater. Interfaces *9*, 2101752.
18. Koshibae, W., and Maekawa, S. (2001). Effects of spin and orbital degeneracy on the thermopower of strongly correlated systems. Phys. Rev. Lett. *87*, 236603.
19. Zhao, L.-D., Lo, S.-H., Zhang, Y., Sun, H., Tan, G., Uher, C., Wolverton, C., Dravid, V.P., and Kanatzidis, M.G. (2014). Ultralow thermal conductivity and high thermoelectric figure of merit in SnSe crystals. nature *508*, 373–377.
20. Son, D.T. (2018). The Dirac composite fermion of the fractional quantum Hall effect. Annu. Rev. Condens. Matter Phys. *9*, 397–411.
21. Du, X., Skachko, I., Duerr, F., Luican, A., and Andrei, E.Y. (2009). Fractional quantum Hall effect and insulating phase of Dirac electrons in graphene. Nature *462*, 192–195.
22. Novoselov, K.S., Geim, A.K., Morozov, S.V., Jiang, D., Katsnelson, M.I., Grigorieva, I.V., Dubonos, S.V., and Firsov, A.A. (2005). Two-dimensional gas of massless Dirac fermions in graphene. nature *438*, 197–200.
23. Castro Neto, A.H., Guinea, F., Peres, N.M.R., Novoselov, K.S., and Geim, A.K. (2009). The electronic properties of graphene. Rev. Mod. Phys. *81*, 109–162.
24. Geim, A.K., and Novoselov, K.S. (2007). The rise of graphene. Nat. Mater. *6*, 183–191.
25. Vogt, P., De Padova, P., Quaresima, C., Avila, J., Frantzeskakis, E., Asensio, M.C., Resta, A., Ealet, B., and Le Lay, G. (2012). Silicene: compelling experimental evidence for graphenelike two-dimensional silicon. Phys. Rev. Lett. *108*, 155501.
26. Dávila, M.E., Xian, L., Cahangirov, S., Rubio, A., and Le Lay, G. (2014). Germanene: a novel two-dimensional germanium allotrope akin to graphene and silicene. New J. Phys. *16*, 095002.
27. Zhu, F.-f., Chen, W.-j., Xu, Y., Gao, C.-l., Guan, D.-d., Liu, C.-h., Qian, D., Zhang, S.-C., and Jia, J.-f. (2015). Epitaxial growth of two-dimensional stanene. Nat. Mater. *14*, 1020–1025.
28. Schoop, L.M., Pielnhofer, F., and Lotsch, B.V. (2018). Chemical Principles of Topological Semimetals. Chem. Mater. *30*, 3155–3176. https://doi.org/10.1021/acs.chemmater.7b05133.
29. Hasan, M.Z., and Kane, C.L. (2010). Colloquium: topological insulators. Rev. Mod. Phys. *82*, 3045–3067.
30. Qi, X.-L., and Zhang, S.-C. (2011). Topological insulators and superconductors. Rev. Mod. Phys. *83*, 1057–1110.
31. Wang, Q., Lei, H., Qi, Y., and Felser, C. (2024). Topological Quantum Materials with Kagome Lattice. Acc. Mater. Res. *5*, 786–796.
32. Bernevig, B.A., Felser, C., and Beidenkopf, H. (2022). Progress and prospects in magnetic topological materials. Nature *603*, 41–51.
33. Wu, C., Bergman, D., Balents, L., and Das Sarma, S. (2007). Flat bands and Wigner crystallization in the honeycomb optical lattice. Phys. Rev. Lett. *99*, 070401.
34. Wu, C., and Das Sarma, S. (2008). $p_{x,\,y}$-orbital counterpart of graphene: Cold atoms in the honeycomb optical lattice. Phys. Rev. B *77*, 235107.
35. Jacqmin, T., Carusotto, I., Sagnes, I., Abbarchi, M., Solnyshkov, D.D., Malpuech, G., Galopin, E., Lemaître, A., Bloch, J., and Amo, A. (2014). Direct observation of Dirac cones and a flatband in a honeycomb lattice for polaritons. Phys. Rev. Lett. *112*, 116402.
36. Landgraf, W., Shallcross, S., Türschmann, K., Weckbecker, D., and Pankratov, O. (2013). Electronic structure of twisted graphene flakes. Phys. Rev. B Condens. Matter *87*, 075433.
37. Guo, H.M., and Franz, M. (2009). Topological insulator on the kagome lattice. Phys. Rev. B *80*, 113102. https://doi.org/10.1103/PhysRevB.80.113102.
38. Mazin, I.I., Jeschke, H.O., Lechermann, F., Lee, H., Fink, M., Thomale, R., and Valentí, R. (2014). Theoretical prediction of a strongly correlated Dirac metal. Nat. Commun. *5*, 4261.
39. Yin, J.-X., Lian, B., and Hasan, M.Z. (2022). Topological kagome magnets and superconductors. Nature *612*, 647–657.
40. Wang, Y., Wu, H., McCandless, G.T., Chan, J.Y., and Ali, M.N. (2023). Quantum states and intertwining phases in kagome materials. Nat. Rev. Phys. *5*, 635–658.
41. Huang, H., Zheng, L., Lin, Z., Guo, X., Wang, S., Zhang, S., Zhang, C., Sun, Z., Wang, Z., Weng, H., et al. (2022). Flat-band-induced anomalous

anisotropic charge transport and orbital magnetism in kagome metal CoSn. Phys. Rev. Lett. *128*, 096601.

42. Ye, L., Kang, M., Liu, J., Von Cube, F., Wicker, C.R., Suzuki, T., Jozwiak, C., Bostwick, A., Rotenberg, E., Bell, D.C., et al. (2018). Massive Dirac fermions in a ferromagnetic kagome metal. Nature *555*, 638–642.
43. Sun, K., Gu, Z., Katsura, H., and Das Sarma, S. (2011). Nearly flatbands with nontrivial topology. Phys. Rev. Lett. *106*, 236803.
44. Kang, M., Ye, L., Fang, S., You, J.-S., Levitan, A., Han, M., Facio, J.I., Jozwiak, C., Bostwick, A., Rotenberg, E., et al. (2020). Dirac fermions and flat bands in the ideal kagome metal FeSn. Nat. Mater. *19*, 163–169. https://doi.org/10.1038/s41563-019-0531-0.
45. Yin, J.-X., Ma, W., Cochran, T.A., Xu, X., Zhang, S.S., Tien, H.-J., Shumiya, N., Cheng, G., Jiang, K., Lian, B., et al. (2020). Quantum-limit Chern topological magnetism in $TbMn_6Sn_6$. Nature *583*, 533–536.
46. Kiesel, M.L., and Thomale, R. (2012). Sublattice interference in the kagome Hubbard model. Phys. Rev. B *86*, 121105.
47. Wilson, S.D., and Ortiz, B.R. (2024). AV_3Sb_5 kagome superconductors. Nat. Rev. Mater. *9*, 420–432.
48. Kiesel, M.L., Platt, C., and Thomale, R. (2013). Unconventional Fermi surface instabilities in the kagome Hubbard model. Phys. Rev. Lett. *110*, 126405.
49. Teng, X., Oh, J.S., Tan, H., Chen, L., Huang, J., Gao, B., Yin, J.-X., Chu, J.-H., Hashimoto, M., Lu, D., et al. (2023). Magnetism and charge density wave order in kagome FeGe. Nat. Phys. *19*, 814–822.
50. Arachchige, H.W.S., Meier, W.R., Marshall, M., Matsuoka, T., Xue, R., McGuire, M.A., Hermann, R.P., Cao, H., and Mandrus, D. (2022). Charge density wave in kagome lattice intermetallic ScV_6Sn_6. Phys. Rev. Lett. *129*, 216402.
51. Xing, Y., Bae, S., Ritz, E., Yang, F., Birol, T., Capa Salinas, A.N., Ortiz, B.R., Wilson, S.D., Wang, Z., Fernandes, R.M., and Madhavan, V. (2024). Optical manipulation of the charge-density-wave state in RbV_3Sb_5. Nature *631*, 60–66.
52. Ye, L., Fang, S., Kang, M., Kaufmann, J., Lee, Y., John, C., Neves, P.M., Zhao, S.F., Denlinger, J., and Jozwiak, C. (2024). Hopping frustration-induced flat band and strange metallicity in a kagome metal. Nat. Phys. *20*, 610–614.
53. Zhou, X., Mandia, D.J., Park, H., Balasubramanian, M., Yu, L., Wen, J., Yakovenko, A., Chung, D.Y., and Kanatzidis, M.G. (2021). New Compounds and Phase Selection of Nickel Sulfides via Oxidation State Control in Molten Hydroxides. J. Am. Chem. Soc. *143*, 13646–13654. https://doi.org/10.1021/jacs.1c05107.
54. Van Miert, G., and Smith, C.M. (2016). Dirac cones beyond the honeycomb lattice: A symmetry-based approach. Phys. Rev. B *93*, 035401.
55. Zhou, X., Wilfong, B., Vivanco, H., Paglione, J., Brown, C.M., and Rodriguez, E.E. (2016). Metastable layered cobalt chalcogenides from topochemical deintercalation. J. Am. Chem. Soc. *138*, 16432–16442.
56. Ayres, J., Berben, M., Duffy, C., Hinlopen, R.D.H., Hsu, Y.-T., Cuoghi, A., Leroux, M., Gilmutdinov, I., Massoudzadegan, M., Vignolles, D., et al. (2024). Universal correlation between H-linear magnetoresistance and T-linear resistivity in high-temperature superconductors. Nat. Commun. *15*, 8406.
57. Analytis, J.G., Kuo, H.H., McDonald, R.D., Wartenbe, M., Rourke, P.M.C., Hussey, N.E., and Fisher, I.R. (2014). Transport near a quantum critical point in $BaFe_2(As_{1-x}P_x)_2$. Nat. Phys. *10*, 194–197.
58. Zhao, H., Zhang, Y., Schlottmann, P., Nandkishore, R., DeLong, L.E., and Cao, G. (2024). Transition between Heavy-Fermion-Strange-Metal and Quantum Spin Liquid in a 4*d*-Electron Trimer Lattice. Phys. Rev. Lett. *132*, 226503.
59. Mozaffari, S., Meier, W.R., Madhogaria, R.P., Peshcherenko, N., Kang, S.-H., Villanova, J.W., Arachchige, H.W.S., Zheng, G., Zhu, Y., Chen, K.-W., et al. (2024). Universal sublinear resistivity in vanadium kagome materials hosting charge density waves. Phys. Rev. B *110*, 035135.
60. Peshcherenko, N., Mao, N., Felser, C., and Zhang, Y. (2024). Sublinear transport in kagome metals: Interplay of Dirac cones and Van Hove singularities. Preprint at arXiv preprint arXiv:2404.11612. https://doi.org/10.48550/arXiv.2404.11612.
61. Bodak, O., Gladyshevskij, E., and Pecharskij, V. (1977). Crystal structure of $CeRe_4Si_2$ compound. Kristallografiya *22*, 178–181.
62. Fu, L., and Kane, C.L. (2007). Topological insulators with inversion symmetry. Phys. Rev. B *76*, 045302. https://doi.org/10.1103/PhysRevB.76.045302.
63. Xia, Y., Qian, D., Hsieh, D., Wray, L., Pal, A., Lin, H., Bansil, A., Grauer, D., Hor, Y.S., Cava, R.J., and Hasan, M.Z. (2009). Observation of a large-gap topological-insulator class with a single Dirac cone on the surface. Nat. Phys. *5*, 398–402.
64. Hussey ||, N.E., Takenaka, K., and Takagi, H. (2004). Universality of the Mott–Ioffe–Regel limit in metals. Philos. Mag. *84*, 2847–2864.
65. Cao, Y., Chowdhury, D., Rodan-Legrain, D., Rubies-Bigorda, O., Watanabe, K., Taniguchi, T., Senthil, T., and Jarillo-Herrero, P. (2020). Strange metal in magic-angle graphene with near Planckian dissipation. Phys. Rev. Lett. *124*, 076801.
66. Keimer, B., Kivelson, S.A., Norman, M.R., Uchida, S., and Zaanen, J. (2015). From quantum matter to high-temperature superconductivity in copper oxides. Nature *518*, 179–186.
67. Balents, L. (2010). Spin liquids in frustrated magnets. Nature *464*, 199–208. https://doi.org/10.1038/nature08917.
68. Chamorro, J.R., McQueen, T.M., and Tran, T.T. (2021). Chemistry of Quantum Spin Liquids. Chem. Rev. *121*, 2898–2934. https://doi.org/10.1021/acs.chemrev.0c00641.
69. Shannon, N., Momoi, T., and Sindzingre, P. (2006). Nematic order in square lattice frustrated ferromagnets. Phys. Rev. Lett. *96*, 027213.
70. Si, Q., and Abrahams, E. (2008). Strong correlations and magnetic frustration in the high T_c iron pnictides. Phys. Rev. Lett. *101*, 076401.
71. Zhu, Y., Gao, T., Fan, X., Han, F., and Wang, C. (2017). Electrochemical techniques for intercalation electrode materials in rechargeable batteries. Acc. Chem. Res. *50*, 1022–1031.
72. Zhou, X., Malliakas, C.D., Yakovenko, A.A., Wilfong, B., Wang, S.G., Chen, Y.-S., Yu, L., Wen, J., Balasubramanian, M., Wang, H.-H., et al. (2022). Coherent approach to two-dimensional heterolayered oxychalcogenides using molten hydroxides. Nat. Synth. *1*, 729–737. https://doi.org/10.1038/s44160-022-00130-4.
73. Zhou, X., Kolluru, V.S.C., Xu, W., Wang, L., Chang, T., Chen, Y.-S., Yu, L., Wen, J., Chan, M.K.Y., Chung, D.Y., and Kanatzidis, M.G. (2022). Discovery of chalcogenides structures and compositions using mixed fluxes. Nature *612*, 72–77. https://doi.org/10.1038/s41586-022-05307-7.
74. Kresse, G., and Furthmüller, J. (1996). Efficient iterative schemes for ab initio total-energy calculations using a plane-wave basis set. Phys. Rev. B *54*, 11169–11186. https://doi.org/10.1103/PhysRevB.54.11169.
75. Kresse, G., and Joubert, D. (1999). From ultrasoft pseudopotentials to the projector augmented-wave method. Phys. Rev. B *59*, 1758–1775. https://doi.org/10.1103/PhysRevB.59.1758.
76. Perdew, J.P., Ruzsinszky, A., Csonka, G.I., Vydrov, O.A., Scuseria, G.E., Constantin, L.A., Zhou, X., and Burke, K. (2008). Restoring the Density-Gradient Expansion for Exchange in Solids and Surfaces. Phys. Rev. Lett. *100*, 136406. https://doi.org/10.1103/PhysRevLett.100.136406.
77. Shao, Y., Molnar, L.F., Jung, Y., Kussmann, J., Ochsenfeld, C., Brown, S.T., Gilbert, A.T.B., Slipchenko, L.V., Levchenko, S.V., O'Neill, D.P., et al. (2006). Advances in methods and algorithms in a modern quantum chemistry program package. Phys. Chem. Chem. Phys. *8*, 3172–3191.
78. Wu, Q., Zhang, S., Song, H.-F., Troyer, M., and Soluyanov, A.A. (2018). WannierTools: An open-source software package for novel topological materials. Comput. Phys. Commun. *224*, 405–416.
79. Pizzi, G., Vitale, V., Arita, R., Blügel, S., Freimuth, F., Géranton, G., Gibertini, M., Gresch, D., Johnson, C., Koretsune, T., et al. (2020). Wannier90 as

a community code: new features and applications. J. Phys. Condens. Matter *32*, 165902.

80. Blöchl, P.E. (1994). Projector augmented-wave method. Phys. Rev. B *50*, 17953–17979. https://doi.org/10.1103/PhysRevB.50.17953.

81. Perdew, J.P., Burke, K., and Ernzerhof, M. (1996). Generalized Gradient Approximation Made Simple. Phys. Rev. Lett. *77*, 3865–3868. https://doi.org/10.1103/PhysRevLett.77.3865.

82. Mao, H.K., Bell, P.M., Shaner, J.W., and Steinberg, D.J. (1978). Specific volume measurements of Cu, Mo, Pd, and Ag and calibration of the rubyR1fluorescence pressure gauge from 0.06 to 1 Mbar. J. Appl. Phys. *49*, 3276–3283. https://doi.org/10.1063/1.325277.

83. Mao, H.K., Xu, J., and Bell, P.M. (1986). Calibration of the ruby pressure gauge to 800 kbar under quasi-hydrostatic conditions. J. Geophys. Res. *91*, 4673–4676. https://doi.org/10.1029/JB091iB05p04673.

84. Prescher, C., and Prakapenka, V.B. (2015). DIOPTAS: a program for reduction of two-dimensional X-ray diffraction data and data exploration. High Press. Res. *35*, 223–230. https://doi.org/10.1080/08957959.2015.1059835.

85. Toby, B.H. (2001). EXPGUI, a graphical user interface for GSAS. J. Appl. Cryst. *34*, 210–213. https://doi.org/10.1107/S0021889801002242.

86. Angel, R.J., Alvaro, M., and Gonzalez-Platas, J. (2014). EosFit7c and a Fortran Module (Library) for Equation of State Calculations. Z. Kristallogr. *229*, 405–419. https://doi.org/10.1515/zkri-2013-1711.